iScience

CellPress
OPEN ACCESS

Article

Improved electrical ideality and photoresponse in near-infrared phototransistors realized by bulk heterojunction channels

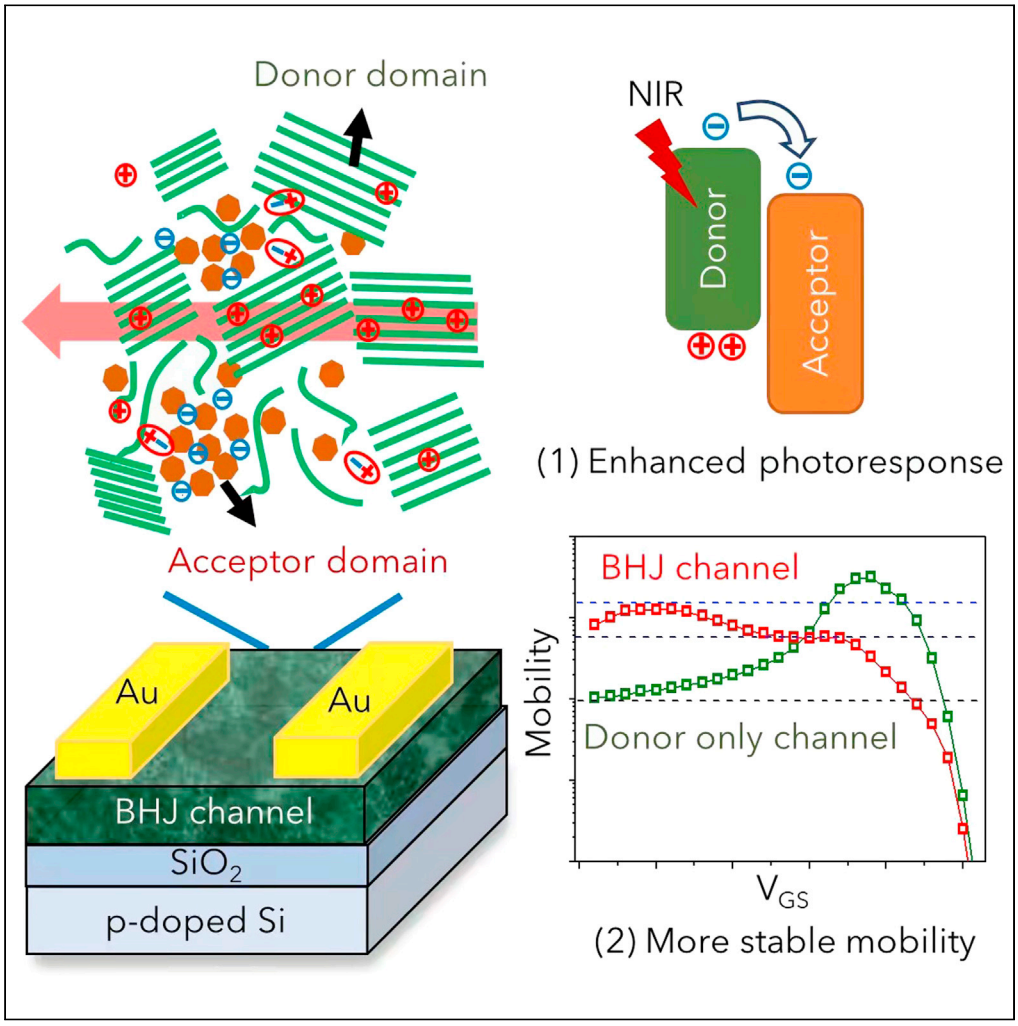

Ning Li, Yanlian Lei, Yanqin Miao, Furong Zhu

miaoyanqin@tyut.edu.cn (Y.M.)
frzhu@hkbu.edu.hk (F.Z.)

Highlights

The use of BHJ channel in NIR OPTs improves the electrical ideality and photoresponse

The acceptor traps injected electrons to maintain the efficient hole transport

The contact resistance in OPTs with BHJ channel is reduced

The better exciton dissociation in BHJ channel offers improved photoresponse

Li et al., iScience 25, 103711
January 21, 2022
https://doi.org/10.1016/j.isci.2021.103711

iScience

CellPress
OPEN ACCESS

Article

Improved electrical ideality and photoresponse in near-infrared phototransistors realized by bulk heterojunction channels

Ning Li,[1] Yanlian Lei,[1,3] Yanqin Miao,[1,2,4,*] and Furong Zhu[1,*]

SUMMARY

The factors that affect the electrical ideality and photoresponse in near-infrared (NIR) organic phototransistors (OPTs) are still nebulous. Here, simultaneous increase in electrical ideality and NIR response in the OPTs is realized by applying a bulk heterojunction (BHJ) channel. The acceptor in the channel helps to trap the undesirable injected electrons, avoiding the accumulation of the electrons at the active channel/dielectric interface, and thereby improving the hole transporting. Use of a BHJ channel also helps reducing the contact resistance in the OPTs. The electrical stability is then improved with mitigated dependence of charge mobility on gate voltage in the saturation region. The BHJ channel also offers an improved photoresponse through enhanced exciton dissociation, leading to more than one order of magnitude increase in responsivity than that in a control OPT. The results are encouraging, which pave the way for the development of high-performing NIR OPTs.

INTRODUCTION

The emerging organic semiconductors have attracted increasing attention for applications in a variety of optoelectronic devices including solar cells, photodetectors, light-emitting diodes, and field-effect transistors (FETs) due to their diverse electrical and optical properties (Benduhn et al., 2017; Fuentes-Hernandez et al., 2020; Guo et al., 2021; Lan et al., 2020; Liu et al., 2020; Wang et al., 2020; Xie et al., 2020; Yokota et al., 2020). The organic photosensitive FETs, also known as the organic phototransistors (OPTs), featuring highly sensitive photoresponse characteristics and ease connection to the readout circuits, have advantages for applications in health monitoring (Knobelspies et al., 2016; Xu et al., 2017), imaging (Hwang et al., 2016; Pierre et al., 2017), gas sensing (Chen et al., 2017; Huo et al., 2015; Li et al., 2019b), and so on. Compared to the traditional inorganic semiconductor materials, organic semiconductors can be prepared by solution-fabrication process, usually enjoy their inherent merits like flexibility and large-area processability for novel optoelectronics (Li et al., 2020; Li et al., 2021a, 2021b). The rapid development of OPTs, benefited from the new material innovation or device optimization, has attracted increasing interests for applications in wearable sensors and high-resolution image sensing (Li et al., 2018, 2019b).

Near-infrared (NIR) OPTs have numerous advances due to figure of merits like ultra-low noise level (Wang et al., 2018; Wei et al., 2018), ultra-high photoresponsivity (Lei et al., 2017; Sun et al., 2012; Xu et al., 2013a, 2017), and nontoxicity as compared to other systems (Gil et al., 2021; Zheng et al., 2020). The active layer in the NIR OPT plays the role as light absorber and charge transport media simultaneously. Thus, parameters including the absorption coefficient (Li et al., 2017), exciton dissociation efficiency (Han et al., 2015; Xu et al., 2013a), and carrier mobility (Kim et al., 2017; Lei et al., 2017; Li et al., 2017) would largely define the performances of the NIR OPTs. Simultaneously, efficient charge photogeneration and charge transport in the active channel are key factors to attain high-performing NIR OPTs (Kim et al., 2017; Lei et al., 2017; Li et al., 2017).

To boost the photoresponse in organic semiconducting systems, photogenerated exciton dissociation plays a key role in photon to charge conversion (Han et al., 2015; Xu et al., 2013a). One strategy is to build an exciton dissociation interface by stacking two active layers forming heterojunction channel configurations (Li et al., 2019c; Park et al., 2009) in OPTs. The multiple-layer heterojunction configuration can be processed by vacuum-based fabrications, but becomes difficult for solution-processed fabrications mainly due

[1]Department of Physics, Research Centre of Excellence for Organic Electronics, and Institute of Advanced Materials, Hong Kong Baptist University, Hong Kong, China

[2]Key Laboratory of Interface Science and Engineering in Advanced Materials of Ministry of Education, Taiyuan University of Technology, Taiyuan 030024, China

[3]School of Physical Science and Technology, Southwest University, Chongqing 400715, China

[4]Lead contact

*Correspondence: miaoyanqin@tyut.edu.cn (Y.M.), frzhu@hkbu.edu.hk (F.Z.)

https://doi.org/10.1016/j.isci.2021.103711

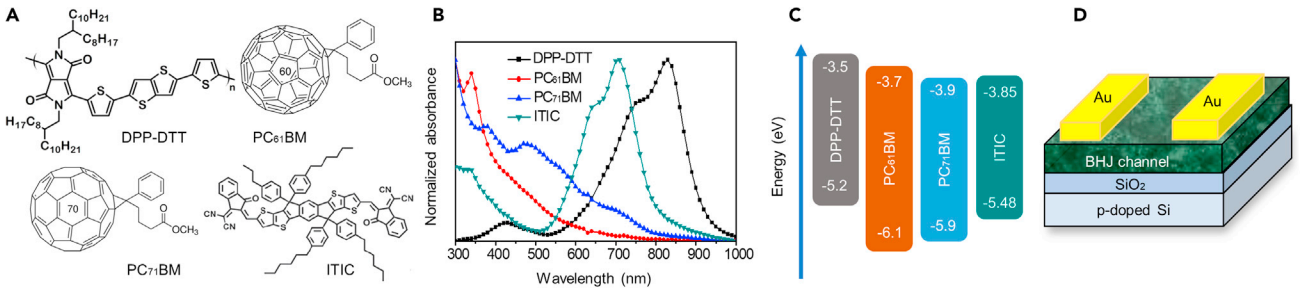

Figure 1. Material properties and device configuration

(A) The molecular structures of the p-type DPP-DTT polymer, and three n-type acceptor materials of $PC_{61}BM$, $PC_{71}BM$, and ITIC.

(B) The normalized absorption spectra of the functional materials.

(C) The schematic energy level diagram of the donor and acceptor materials used in this work.

(D) The schematic cross-sectional view of the OPT with a bottom-gate top-contact configuration.

to the solvent damage by subsequent coating (Kim et al., 2019a; Li et al., 2019c). An alternative strategy is to prepare material blends where percolating interfaces are favorable for exciton dissociation and separation. This method is well developed in high-performing organic solar cells where donors and acceptors are blended forming a bulk heterojunction (BHJ) in the cells (Han et al., 2015; Xu et al., 2013a). The photogenerated exciton can be disassociated efficiently at the donor/acceptor (D/A) interface, which gives rise to much enhanced photon to electron conversion (Heeger, 2014; Park et al., 2009; Scharber et al., 2006).

Meanwhile, it is found that the introduction of n-type acceptor into the p-type channel in organic FETs (OFETs) helps to relieve the nonideality of the transfer curves. The carrier mobility of the OFETs in the saturation region varies significantly with the gate voltage, known as the nonideality of the charge transport in the OFETs (Bittle et al., 2016; Luo et al., 2014; Phan et al., 2015, 2017, 2018; Sirringhaus, 2014), is bringing considerably attention because the nonideality will affect the device operation stability (Phan et al., 2017). The nonideality of the OFET featuring "double slope" of the transfer curves may result in the overestimation of carrier mobility, which deviates from the idealized model (Bittle et al., 2016). The reasons causing the nonideality in OFETs include contact resistance, as well as the existence of traps at the silicon dioxide dielectric/channel interface (Phan et al., 2017) that affects charge transport in the channel. However, the effect of the acceptors in the BHJ channel on the electrical and photoresponse properties of the NIR OPTs is still nebulous. The relation between material miscibility and film morphology is not clearly understood yet.

In this work, we examined both the electrical ideality and optical response in NIR OPTs by analyzing the current–voltage characteristics and studying the donor/acceptor interaction in the BHJ channel. The use of a BHJ channel helps mitigating the gate-bias-dependent mobility, revealing an uninterrupted charge transport near the channel/dielectric interface. The current–voltage characteristics in transistors with improved ideality fit well with the theoretical model. It is also found that incorporation of an optimal acceptor in the BHJ channel is essentially important not only to retain the good crystallinity of the donor polymer but also to provide efficient photogenerated exciton dissociation, resulting in improved charge photogeneration and collection, thus much higher photoresponse.

RESULTS AND DISCUSSION

The BHJ channels in the OPTs comprise the donor polymer diketopyrrolopyrrole-dithienylthieno[3,2-b] thiophene (DPP-DTT) and fullerene derivatives of $PC_{61}BM$, $PC_{71}BM$, and non-fullerene acceptor ITIC. The molecular structures of the materials are schematically illustrated in Figure 1A. Their respective absorption spectra are shown in Figure 1B. It is clear that the DPP-DTT layer is sensitive to NIR light with a peak absorption located at ~830 nm. DPP-DTT is also proven to be a high hole mobility polymer and is suitable for high-performance FETs with a low subthreshold swing and a high on/off ratio (Lei et al., 2016a, 2016b; Li et al., 2012). These promising optoelectronic characteristics of the DPP-DTT polymer are also attractive for NIR detection and image sensing (Li et al., 2018).

In this study, three different BHJ channel layers of DPP-DTT:$PC_{61}BM$, DPP-DTT:$PC_{71}BM$, and DPP-DTT:ITIC, were used for making the NIR OPTs. The polymer donor and acceptor form type II heterojunction

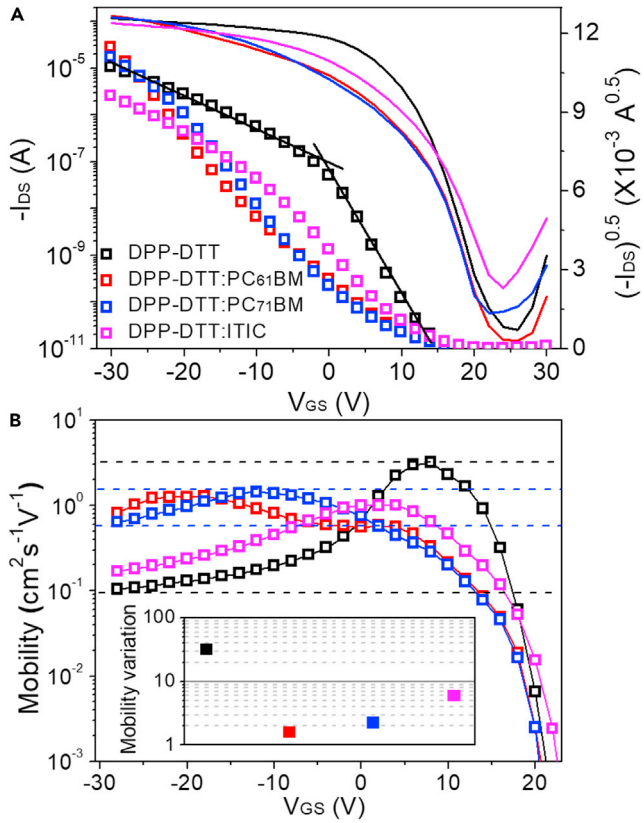

Figure 2. The electrical characteristics of the OPTs

(A) The dark I_{DS}−V_{GS} transfer curves and the corresponding I_{DS} values. V_{DS} was set at −30 V. The double-slope feature in the semilogarithmic I_{DS}−V_{GS} curves of the control OPT with a pristine DPP-DTT channel is denoted using two straight solid lines.

(B) Calculated V_{GS}-dependent carrier mobility using the values presented in (A). The inset in (B) is the mobility variation factor, a ratio of the peak mobility to the minimum mobility (at V_{GS} = −30 V) in the saturation region of the OPTs with different channel layers.

(Osedach et al., 2010), as shown in Figure 1C, which is favorable for photogenerated exciton dissociation. The NIR OPT is schematically shown in Figure 1D, in a bottom-gate top-contact structure. The OPTs with a pristine DPP-DTT channel also were fabricated as control devices for comparison study.

The electrical characteristics of the phototransistor, e.g., transfer properties and mobility, were investigated. In Figure 2A, the source-drain current (I_{DS}) as a function of source-gate voltage (V_{GS}) of the OPTs comprising different channels was shown and their corresponding $\sqrt{I_{DS}} - V_{GS}$ characteristics were presented as well. The source-drain voltage V_{DS} was set at −30V. These OPTs show good p-type transfer characteristics with ~10^6 on–off ratios. To estimate the saturated mobility (μ_{sat}) of carriers in the transistors, one can employ the equation as described in Equation 1.

$$\mu_{sat} = \frac{2L}{WC_i}\left(\frac{\partial\sqrt{I_{DS}}}{\partial V_{GS}}\right) \qquad \text{(Equation 1)}$$

L and W are the channel length and width, C_i is the capacitance per unit area of the gate dielectric. The slope of $\sqrt{I_{DS}}$ against V_{GS} decides the carrier mobility. The model for the calculation of the saturated mobility assumes the mobility is independent of V_{GS} (Phan et al., 2018). However, as shown in Figure 2A, a double-slope behavior with a kink at V_{GS} = 0V was observed in a control OPT with a pristine DPP-DTT channel, resulting in non-stable carrier mobility in the saturation region. The mobility calculated from low V_{GS} is higher than that from high V_{GS} range, which might cause overestimation in charge carrier mobility (Bittle et al., 2016). The double-slope feature in $\sqrt{I_{DS}}$ versus V_{GS} plot is associated to the non-ideality in the OFETs (Bittle et al., 2016; Phan et al., 2018). The non-stable mobility in the saturation region would give rise

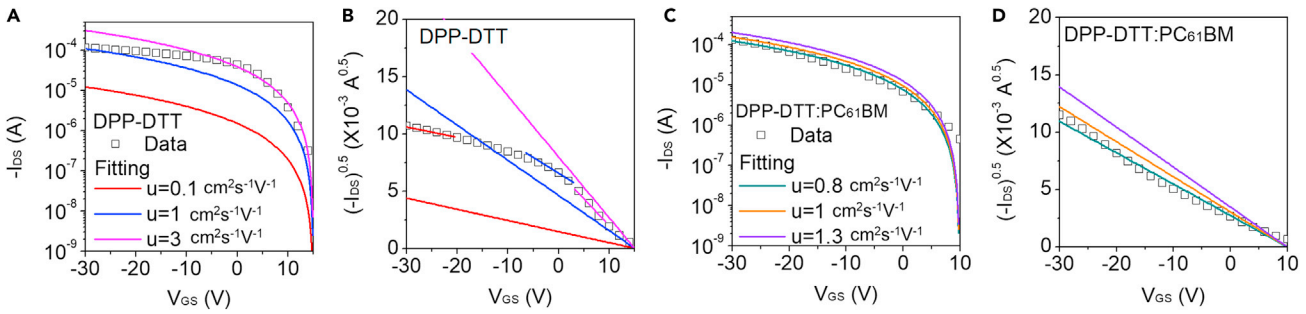

Figure 3. The comparison between measured electrical signal and theoretical model

(A) I_{DS}–V_{GS} transfer curves measured for a control OPT with a pristine DPP-DTT channel and the ones calculated using different mobility values adopted in the ideal model.

(B) $\sqrt{I_{DS}} - V_{GS}$ characteristics obtained using the measured and theoretical simulation results. In the calculation, three different mobility values of 0.1, 1.0, and 3.0 $cm^2s^{-1}V^{-1}$ were used.

(C and D) I_{DS}–V_{GS} transfer curves measured for an OPT with a DPP-DTT:PC_{61}BM-based BHJ channel and (D) $\sqrt{I_{DS}} - V_{GS}$ characteristics obtained using the measured and theoretical simulation results. Three different mobility values of 0.8, 1, and 1.3 $cm^2s^{-1}V^{-1}$ were used in the simulation. V_{DS} of −30 V was used in the measurements.

to unstable operation of the transistor. As a comparison, the transistors with different BHJ channel layers exhibit much less double-slope phenomenon, especially in the transistors with a BHJ channel comprising the fullerene acceptor and its derivatives. The V_{GS}-dependent mobility was calculated using Equation 1 and the results were presented in Figure 2B.

The mobility in DPP-DTT transistors shows a clear plateau at around V_{GS} = 5 V, manifesting huge mobility fluctuation in the saturation region. On the contrary, the mobility in transistors with BHJ channel comprising different fullerene acceptors shows much mitigated variation in the saturation region. To compare the change of mobility as a function of V_{GS} in the saturation region, the mobility variation factor, defined as the ratio of peak mobility over the mobility at V_{GS} = −30V, for the OPTs with different channel layers were plotted in the inset of Figure 2B. The variation in the charge carrier mobility of a control OPT with a pristine DPP-DTT channel in the saturation region is 30 times larger than that of the OPTs with BHJ channels comprising fullerene derivative acceptors. It is thus clear that incorporation of an optimal amount of the acceptor molecules in the DPP-DTT donor polymer helps mitigating the non-ideality of the mobility in the OPTs.

To make a clear comparison between the measured transfer curves and the ideal ones calculated based on the model, as described by Equation 1, we conducted the calculation by varying the carrier mobility to fit the experimental data. The channel current I_{DS} can be described as Equation 2, which is derived from Equation 1.

$$I_{DS} = \mu_{sat} C_i \frac{W}{2L} (V_{GS} - V_{th})^2 \qquad \text{(Equation 2)}$$

I_{DS}-V_{GS} transfer curves measured for a control OPT with a pristine DPP-DTT channel and an OPT with a DPP-DTT:PC_{61}BM-based BHJ channel are compared with the data calculated using Equation (2). From the V_{GS} dependent mobility provided in Figure 2B, the mobility values of a control OPT with a pristine DPP-DTT channel are in the range of 0.1–3 $cm^2s^{-1}V^{-1}$, while the mobility values of the OPT with a DPP-DTT:PC_{61}BM-based BHJ channel is more stable, ranging from 0.8 to 1.3 $cm^2s^{-1}V^{-1}$. To fit the experimental data, we plotted I_{DS}–V_{GS} curves calculated for the control OPT with a pristine DPP-DTT channel using three different mobility values of 0.1, 1, and 3 $cm^2s^{-1}V^{-1}$ and the ones calculated for the OPTs with a DPP-DTT:PC_{61}BM BHJ channel using three different mobility values of 0.8, 1, and 1.3 $cm^2s^{-1}V^{-1}$. The other parameters in the model were kept the same in the fitting process. I_{DS}–V_{GS} transfer curves and $\sqrt{I_{DS}} - V_{GS}$ characteristics obtained from experimental and modeling results are shown in Figure 3. The theoretical simulation is consistent with the measured results, indicated by the slopes in the I_{DS}–V_{GS} characteristics. However, the instable mobility values in DPP-DTT OPTs lead to discrepancy between the measured data and the model, as shown in Figures 3A and 3B. Three discrete lines were indicated in Figure 3B to show the slope variation, which show the mobility instability at different V_{GS}. As a comparison, the results measured for the OPT with a DPP-DTT:PC_{61}BM-based BHJ channel fit better with the model, due to a small

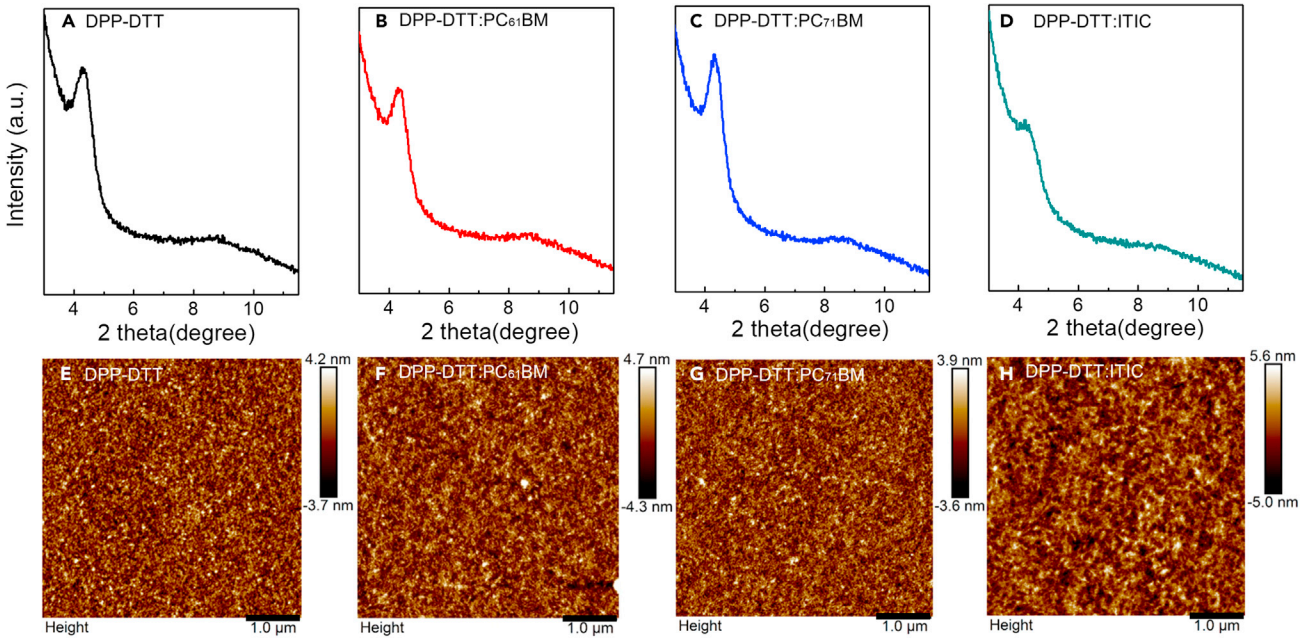

Figure 4. The molecular packaging and morphological properties of the channel films

(A–H)The XRD results measured for (A) DPP-DTT, (B) DPP-DTT:$PC_{61}BM$, (C) DPP-DTT:$PC_{71}BM$, and (D) DPP-DTT:ITIC thin films prepared on SiO_2. The AFM images measured for different thin films of (E) DPP-DTT, (F) DPP-DTT:$PC_{61}BM$, (G) DPP-DTT:$PC_{71}BM$, and (H) DPP-DTT:ITIC.

variation in mobility, as shown in Figures 3C and 3D. These data clearly show the electrical non-ideality phenomenon in DPP-DTT transistors, which also exists in different OFETs. The idea to incorporate a proper acceptor to form BHJ for the channel in the transistor paves the way for improved electrical ideality, which is meaningful in the design of stable transistors.

To investigate the effect of different acceptors on the molecular packing and morphology of the BHJ channel, X-ray diffraction (XRD) and atomic force microscopy (AFM) measurements were conducted. The respective XRD patterns measured for the DPP-DTT, DPP-DTT:$PC_{61}BM$, DPP-DTT:$PC_{71}BM$, and DPP-DTT:ITIC films are presented in Figures 4A–4D, and all show the typical diffraction peak of the DPP-DTT donor material. Compared to the XRD patterns measured for a pristine DPP-DTT layer, there is a negligible change in the peak intensity of the XRD patterns measured for the layers prepared using the DPP-DTT blended with different fullerene derivatives, indicating the DPP-DTT in the BHJ remained good crystallinity. While in the DPP-DTT:ITIC blend film, the diffraction intensity decreased, indicating an obvious change in the molecular packaging of DPP-DTT. The decrease in molecular packing of the donor material will lead to deteriorated carrier mobility, affecting the photogenerated charge transport and collection. The reduced XRD intensity also indicates a possible poor miscibility between DPP-DTT and ITIC.

Further, the AFM measurements were conducted to test the morphology change after the incorporation of different acceptors. The results are shown in Figures 4E–4H. The root-mean-square roughness measured for the DPP-DTT, DPP-DTT:$PC_{61}BM$, DPP-DTT:$PC_{71}BM$, and DPP-DTT:ITIC films are 1.1, 1.3, 1.0, and 1.5 nm, respectively. The BHJ film comprising $PC_{71}BM$ has a much less change in morphology as compared to the pristine DPP-DTT film, indicating a good miscibility between the donor polymer and acceptor. The DPP-DTT and ITIC materials are not well mixture in the precursor solution, which is probably the reason for relatively poor electrical ideality in the transistor with a DPP-DTT:ITIC BHJ channel, due to their poor miscibility. Overall, mixing with fullerene derivative acceptors has less impact on the molecular packing and morphology properties of the DPP-DTT polymer.

The reasons of nonideality in a transistor are still not fully understood (Phan et al., 2018). The improved ideality of the OPTs with a BHJ channel having fullerene derivative is mainly due to its electrical properties. We have evaluated the contact resistance (R_C) of the OPTs made with different channel layers. The results are shown in Figure S1. The contact resistance obtained for a control OPT with a pristine DPP-DTT channel

layer, and the OPTs with three different BHJ channel layers of DPP-DTT:$PC_{61}BM$, DPP-DTT:$PC_{71}BM$, and DPP-DTT:ITIC are 0.9, 0.74, 0.45, 0.8 mega-ohms, respectively. Obviously, the contact resistance in a control OPT with a pristine DPP-DTT channel is slightly higher than the ones in the OPTs with a BHJ channel. Our results support the previous observation in showing that a higher contact resistance is also responsible for the electrical nonideality in the OPTs, because incorporation of the acceptor molecules in the channel reduced the contact resistance and thus mitigates the fluctuation of the gate-voltage-dependent mobility in the saturation region.

The contact resistance in a transistor is an important factor affecting the electrical ideality of the transistor (Bittle et al., 2016; Liu et al., 2017; McCulloch et al., 2016). A 10-fold overestimation in mobility of the transistor can be occurred if a Schottky contact exists at the electrode/channel interface (Liu et al., 2017), agreeing with the variation of the mobility we have observed in the control OPT with a pristine DPP-DTT channel, as shown in Figure 2B. The existence of the contact resistance disturbs the charge injection at a low gate voltage region, causing a discrepancy in the estimation of the charge mobility using standard MOSFET models (Bittle et al., 2016). In a practical perspective, detailed modeling complying the real situation is required for accurate determination of the mobility (McCulloch et al., 2016). The contact resistance often results in a gradually downward in the transfer curves (Braga and Horowitz, 2009; Phan et al., 2018). However, it is not easy to distinguish the downward-sloping features and double-slope characteristics because they are fairly similar (Phan et al., 2018). As a result, it is more appropriate to discuss the nonideality in electrical properties in an OFET considering all the possible causes.

Another hypothesis to interpret the electrical nonideality is the electron trapping at the channel/dielectric interface. It has been reported that the presence of moisture or oxygen at the SiO_2 surface would affect the charge transport in the channel (Bobbert et al., 2012; Nikolka et al., 2017), because the transfer of the charges basically takes place near the vicinity of the dielectric/channel interface (Kim et al., 2013). Although the surface of the SiO_2 dielectric layer was modified with trichloro(octadecyl)silane in our case, the surface probably still has some residual electron trap states, such as silanol groups (SiOH) (Chua et al., 2005), which would capture and trap the injected electrons. Most of the double-slope nonideality of the electrical properties in OFETs occurs in devices having a SiO_2 dielectric layer, even after self-assembled monolayer treatment (Phan et al., 2017). The electron trapping at the dielectric surface (Aguirre et al., 2009; Chua et al., 2005) would lead to the electrical instability featuring double-slope phenomenon (Phan et al., 2015, 2017).

Polymers with the donor–acceptor (D-A) structural units usually have a lowest unoccupied molecular orbital (LUMO) below −3.5 eV, which potentially allows electron injection and transport (Newman et al., 2004), leading to ambipolar charge transport (Zaumseil and Sirringhaus, 2007). The DPP-DTT polymer used in this work has a D-A configuration with an LUMO of −3.5 eV, which potentially allows electron injection and transport. We do observe n-type charge transport in our OFETs from the transfer curves at large positive V_{GS}. The narrow bandgap of the p-type polymer is vulnerable to electron injection. We then performed the electron current decay under bias-stress (electron accumulation region with positive V_{GS}). The results are shown in Figure S2. It is clear that the electron current decay in the OFET with a DPP-DTT channel is more significant, indicating a more serious electron trapping at the channel/dielectric interface (Phan et al., 2015, 2018).

Different approaches were proposed to resolve the double-slope nonideality in the OFETs, for example, creating an ohmic contact between the channel and channel through eliminating the contact resistance using an energy level matching buffer layer. The other way is to diminish electron trapping at the channel/dielectric interface. Methods such as using a highly hydrophobic polymer dielectric, to eliminate the traps at the dielectric/channel interface (Phan et al., 2015) were also reported. Incorporation of different acceptors with a high electron affinity in the channel to trap the electrons, injected from the source-drain electrodes, is an effective way to avoid electron trapping near the dielectric (Phan et al., 2017). In this work, we show that the use of a BHJ channel helps improving the electrical ideality of the OPTs through the combined advantages of (1) reduced contact resistance and (2) suppression of the electron trapping at the channel/dielectric interface.

The use of a BHJ channel in the OPTs not only improves the electrical ideality but also enhances the optical photoresponse. The transfer curves measured for the OPTs without and under NIR light illumination were presented in Figures 5A–5D. The source-drain voltage V_{DS} was fixed at −30 V while the gate-source voltage

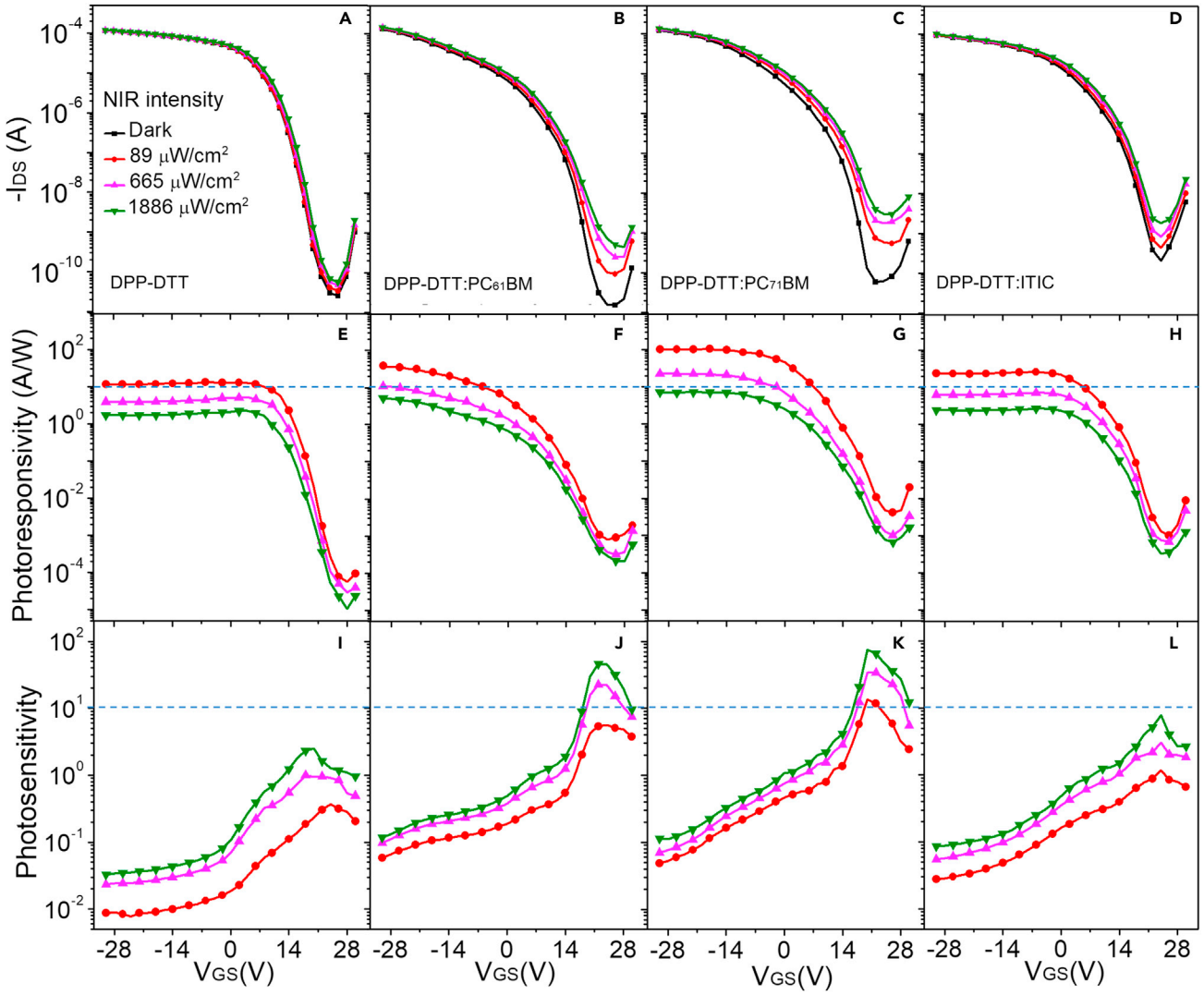

Figure 5. NIR (850 nm) photoresponse of the OPTs with different channels

(A–L)The transfer curves measured for (A) a control OPT with a pristine DPP-DTT channel, and the OPTs with different BHJ channel layers of (B) DPP-DTT:$PC_{61}BM$, (C) DPP-DTT:$PC_{71}BM$, and (D) DPP-DTT:ITIC in the dark and under illumination with different NIR light intensities. The photoresponsivity measured for (E) a control OPT with a pristine DPP-DTT channel, and the OPTs with different BHJ channel layers of (F) DPP-DTT:$PC_{61}BM$, (G) DPP-DTT:$PC_{71}BM$, and (H) DPP-DTT:ITIC. The photosensitivity results measured for (I) a control OPT with a pristine DPP-DTT channel, and the OPTs with different BHJ channel layers of (J) DPP-DTT:$PC_{61}BM$, (K) DPP-DTT:$PC_{71}BM$, and (L) DPP-DTT:ITIC. V_{DS} of −30 V was used in the measurements.

V_{GS} was scanned from 30 V to −30 V. Charge photogeneration occurs under NIR light illumination, which increases the carrier density in the OPT channel, resulting in the increment of I_{DS}. From the transfer curves, the OPTs with three different BHJ-based channels show a better photoresponse as compared to that of a control OPT with a pristine DPP-DTT channel. Photoresponsivity (R) defined as $R = I_{photo}/P_{incident}$, where I_{photo} and $P_{incident}$ are the photocurrent and incident light power, respectively, is one of the key factors to evaluate the photoresponse performance. Clearly in Figures 5E–5H, the OPTs with different BHJ channels show higher photoresponsivity than that in a control OPT with a pristine DPP-DTT channel layer. Under the NIR light intensity of $89 \mu W/cm^2$, the best photoresponsivity of the OPTs with three different BHJ channels of DPP-DTT:$PC_{61}BM$, DPP-DTT:$PC_{71}BM$, and DPP-DTT:ITIC were 38, 104, and 26 A/W, which is higher than that observed for a control OPT with a pristine DPP-DTT channel (13 A/W).

From the photoresponsivity plots, it is also observed that there is a clear saturation feature or even reduced R as $|V_{GS}|$ increases in the OPTs, with different channel layers of DPP-DTT and DPP-DTT:ITIC, in the saturation region,

which is most probably due to the mobility decrease as $|V_{GS}|$ gets higher as shown in Figure 2B. This phenomenon was also observed in different OPTs with a single-component channel layer in literatures (Guo et al., 2009; Liu et al., 2014; Yu et al., 2013; Zhu et al., 2016). The nonideality in the electrical property of the transistor would be one of the most probable reasons. The relation between electrical ideality and photoresponsivity is close as observed in this work, but there are few reports in literature so far. The results in this work would be of great importance for the design of stable and high-performing optical OPTs.

The light-intensity-dependent photoresponsivity in the phototransistors is usually associated with the presence of trap states (Kim et al., 2019b), the inherent characteristics of the low disordered functional materials. The long lifetime of the deep traps is the main reason enabling the photoconductive gain in a phototransistor. However, under high light intensity, the phototransistor has a relatively reduced gain, and thereby a lower photoresponsivity, due to the saturation of the deep traps filled by the large amount of the photogenerated charges in the active layer.

Another important characteristic for a detector is the specific detectivity (D^*), which represents the detection limits. It is defined as $D^* = R\sqrt{A}/S_n$, where R is the photoresponsivity, A is the active area, and S_n is the noise spectral density. The unit for $D^*$is $cm \cdot \sqrt{Hz}/W$, or Jones while$A/\sqrt{Hz}$ is the unit for S_n. Once the noise current is dominated by dark charge injection, the main noise source in a detector becomes shot noise, which stems from dark current. The noise can be expressed in $S_n = 2q\sqrt{I_{dark}}$, where q is the elementary charge and I_{dark} is the dark current of the detector. In Figure S3, the D^* for the control OPT with a pristine DPP-DTT channel and the OPTs with different BHJ channel layers is presented. The photoresponsivity and dark current are from Figure 5. The NIR light intensity is 89 $\mu W/cm^2$. The D^* is dependent on light intensity and bias. Higher photoresponsivity and lower noise current are essential factors for attaining a higher D^*. Clearly, the D^* of the OPT with a DPP-DTT:$PC_{71}BM$-based BHJ channel layer is higher, exceeding 10^{12} Jones, which is mainly due to a much higher photoresponsivity.

The photosensitivity (P) is defined as $P = I_{photo}/I_{dark}$, where I_{photo} represents the photocurrent and I_{dark} is the dark current. The photosensitivity of a detector represents the capability in identifying signal from noise. The photosensitivity of the OPTs is presented in Figures 5I–5L. Consistent with the photoresponsivity, the photosensitivity of the OPT with a DPP-DTT:$PC_{71}BM$-based BHJ channel layer is highest, which is more than one order of magnitude larger than that of the control OPT with a pristine DPP-DTT channel layer. This is again due to a much-enhanced photocurrent generation in the BHJ under NIR light.

The photoresponse of a detector relies on a number of parameters, e.g., light absorption, photogenerated exciton dissociation, and photogenerated charge collection. The enhanced NIR photoresponse in the OPTs with a BHJ channel layer, especially in the DPP-DTT polymer channel incorporating $PC_{71}BM$, is mainly attributed to the better exciton dissociation and charge separation at the donor/acceptor interface and stable charge mobility in the saturation region. In the DPP-DTT:$PC_{71}BM$ BHJ, the good crystallinity of the donor polymer remains and the morphological change is negligible as compared to the pristine donor thin film, indicating a good miscibility between the polymer donor and the fullerene acceptor. In such a situation, the hole transport in the polymer domain will not be affected by the acceptor material. To unravel the improved photoresponse in the DPP-DTT:$PC_{71}BM$ PT, the exciton dissociation at the D/A interface was studied by analyzing the photoluminescence (PL) characteristics of the BHJ film.

The steady-state PL spectrum of a $PC_{71}BM$ layer as a function of wavelength was measured. The PL peak was located at 710 nm as shown in Figure 6A. The time-resolved PL was then conducted for $PC_{71}BM$ film and DPP-DTT:$PC_{71}BM$ BHJ film by illuminating 325 nm light onto the films and recording signals at 710 nm. The results are shown in Figure 6B. Because the activation laser is at 325 nm, the activation light is supposed to be mostly absorbed by the acceptor materials because the DPP-DTT donor has a negligible absorption at such wavelength, as shown in Figure 1B. The time-resolved PL signal was fitted using the exponential equation (Qian et al., 2018; Shen et al., 2016) in the form of $F(t) \propto e^{-t/\tau}$ (Li et al., 2019a; Pham et al., 2017), where τ represents the PL lifetime of the charge carriers. The PL lifetime calculated for $PC_{71}BM$ and DPP-DTT:$PC_{71}BM$ blend was 0.33 and 0.21 ns, respectively. The PL results reveal an efficient exciton dissociation and charge separate at the D/A interface in the OPTs with a DPP-DTT:$PC_{71}BM$-based channel. The photogenerated excitons disassociate at the D/A interface and the holes generated in the acceptor phase tend to transfer from the acceptor to the donor; therefore, the emissive recombination in the acceptor was suppressed and the PL lifetime was shortened (Qian et al., 2018).

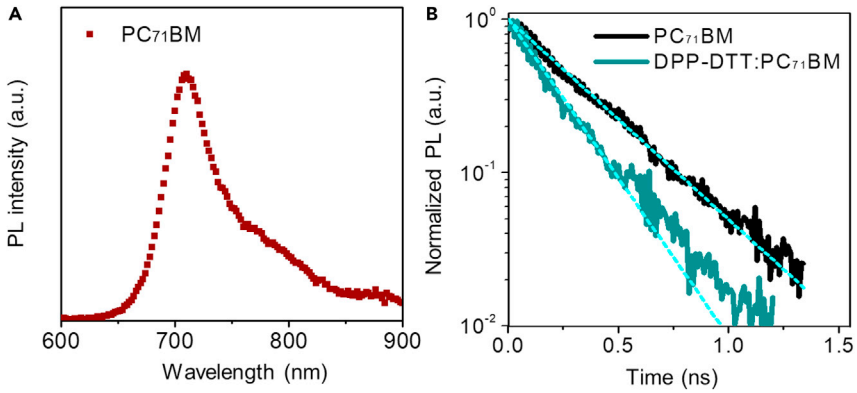

Figure 6. Photoluminescence characteristics

(A and B) The steady-state PL spectrum measured for a 40 nm thick $PC_{71}BM$ layer, with a PL peak located at 710 nm. The time-resolved PL spectra measured for (B) a 40 nm thick $PC_{71}BM$ layer and a 50 nm thick DPP-DTT:$PC_{71}BM$ blend layer. The PL signal was collected at 710 nm. The solid lines represent the fitting data.

Based on these results, the high performance in DPP-DTT:$PC_{71}BM$ NIR OPTs can be attributed to efficient photogenerated exciton dissociation and stable channel mobility for the transportation and collection of photogenerated charges. The schematic illustration showing the mechanisms were shown in Figure S4. Under NIR light illumination, photogenerated excitons are formed in the donor material through absorption. The excitons get dissociated and separated efficiently at the D/A interface in the DPP-DTT:$PC_{71}BM$ BHJ as schematically illustrated in Figure S4A. $PC_{71}BM$ has a high electron affinity as compared to other acceptor materials, such that the photogenerated electrons can be attracted and trapped in the acceptor domain, allowing multiple hole collection through the crystalline DPP-DTT domain (Yu et al., 2016), as shown in Figure S4B. The slow de-trapping of photogenerated electrons in the $PC_{71}BM$ domain and fast and stable hole transport in the crystalline DPP-DTT domain are responsible for the high NIR light detection capability in the OPT with a DPP-DTT:$PC_{71}BM$-based BHJ channel. In such a mechanism, photomultiplication gain is readily achieved, manifesting external quantum efficiency (*EQE*) higher than 100% (gain>1). The *EQE* can be calculated by $EQE = R \cdot h\nu$, where $h\nu$ is the incident photon energy in eV. In this work, a photoresponsivity of 104 A/W and an *EQE* of 15,184% were obtained for the NIR OPT with a DPP-DTT:$PC_{71}BM$ channel layer.

In Figure 7, the transient photoresponses of the OPTs with different channel layers are presented. The NIR light signal (850 nm) was chopped at a frequency of ~0.5 Hz. The NIR light intensity was set at 100 $\mu W/cm^2$. The V_{GS} and V_{DS} were fixed at −5.0 V and −30 V, respectively, in the measurements. As a comparison, the NIR OPT with a DPP-DTT:$PC_{71}BM$-based BHJ channel is evidently more sensitive than that of the OPTs with a pristine DPP-DTT channel and two different BHJ channels of DPP-DTT:$PC_{61}BM$ and DPP-DTT:ITIC. The rise and fall time estimated for the OPT with a DPP-DTT:$PC_{71}BM$ BHJ channel are 20 ms and 350 ms, respectively, which are faster than that of the control OPT with a pristine DPP-DTT channel (Lei et al., 2017), due to the fast charge separation in the BHJ channel. The fall time is much slower than the rise time, which is mostly due to the slow detrapping process caused by the electron traps (Xu et al., 2013b).

There is a shift in the dark current of different OPTs, as presented in Figure 7. This change in the dark current is related to the bias stress (Ng et al., 2007; Rim et al., 2015a). Organic semiconductors are more disordered as compared to the inorganic semiconductors, with plenty of inherent charge traps. The change in the dark current in the OPTs is closely associated with the presence of the charge traps in the active layer. The reduction in the number of the mobile carriers, trapped either at the dielectric/semiconductor interface or inside the active layer, in an OPT operated under a bias is responsible for the reduced device current. It is also possible that new traps can be created during the operation (Ng et al., 2007). The proper interfacial engineering and optimal device fabrication processes are required, including dedicated channel/dielectric modification, oxygen and humidity control, and so on.

The stability and reproducibility of the NIR OPTs prepared in this work have been examined. The DPP-DTT polymer is pretty stable in air with oxygen and humidity. It is printable in ambient atmosphere with comparable electrical performance to that processed in inert atmosphere (Lei et al., 2016b). In this work, the

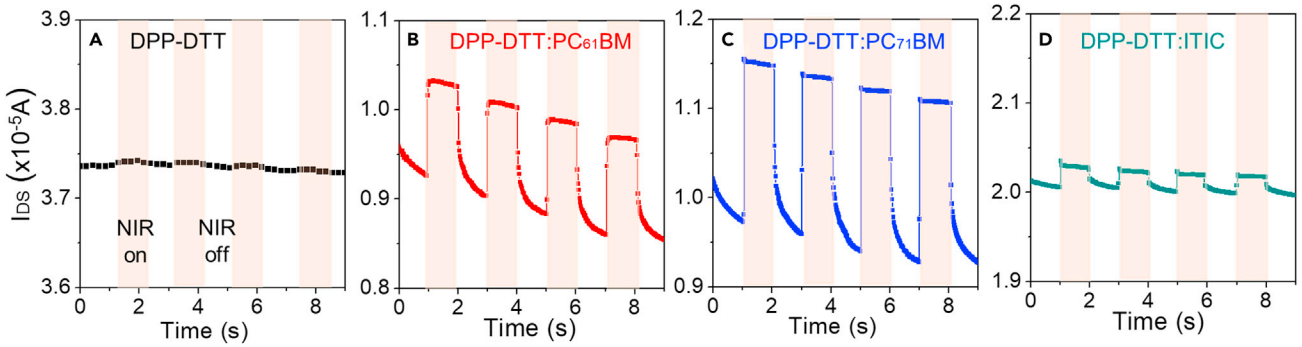

Figure 7. Transient photoresponses of the NIR OPTs

(A–D)The transient response measured for the NIR OPTs with different channel layers of (A) DPP-DTT, (B) DPP-DTT:$PC_{61}BM$, (C) DPP-DTT:$PC_{71}BM$, and (D) DPP-DTT:ITIC. V_{GS} of −5 V, V_{DS} of −30 V, and an NIR (850 nm) light intensity of 100 $\mu W/cm^2$ were used in the measurements.

blend layer with a ratio of DPP-DTT to acceptor of 2:1 was used for making the BHJ channel layer in the OPTs. The lower ratio of the acceptor in the BHJ layer allows the acceptor molecules being wrapped and protected by the air stable DPP-DTT molecules. In our previous study, we observed that the hydrophobic surface of the DPP-DTT polymer (Li et al., 2019c) has the advantage of retarding the permeation of oxygen and moisture to the channel in the OPTs.

The durability of the NIR OPTs has been analyzed through monitoring both the dark current and photocurrent of the OPTs over a period of 10 days. The devices were stored in a dry box in the air without any encapsulation. As shown in the Figure S5, there is no obvious change in the electrical and optical properties in the control OPT with a pristine DPP-DTT channel and the OPT with a DPP-DTT:$PC_{71}BM$-based BHJ channel. The photoresponsivity in the OPT with a DPP-DTT:$PC_{71}BM$ BHJ channel dropped about 10% from its initial value, which is most probably due to the fact that $PC_{71}BM$ is sensitive to oxygen and humidity, which can be minimized using a proper encapsulation.

The performance repeatability of the OPTs demonstrated in this work is very encouraging. The dark transfer curves and photoresponsivity characteristics measured for the control OPT with a pristine DPP-DTT channel and the OPT with a DPP-DTT:$PC_{71}BM$-based BHJ channel are presented in Figure S6. The error bars donate the distribution of the standard deviation from the measurements of 9 devices. There is a very small variation in the performance of the OPTs prepared in different batches, especially the OPTs with a DPP-DTT:$PC_{71}BM$-based BHJ channel have a very reliable performance reproducibility. The photoresponse of the NIR OPTs was measured under the illumination with an NIR (850 nm) light intensity of 89 $\mu W/cm^2$.

The use of a BHJ channel in an OPT is essential for charge photogeneration, thus improving the overall photodetection performances (Han et al., 2015; Nam et al., 2016; Xu et al., 2013b, 2016). However, the sense of seeking a proper donor/acceptor heterostructure to simultaneously improve the electrical ideality and optical response is not well established. We report here that miscibility of the donor and acceptor, and morphology of the channel are key factors that impact on the electrical ideality and optical response of the OPTs. Incorporation of nanostructures, e.g., photonic structures and quantum dots, in the photoactive layer would help to achieve absorption enhancement in OPTs, thereby improving the sensitivity of the NIR detection. It is anticipated that a combination of theoretical simulation and experimental optimization will offer a facile approach toward achieving high-performance solution-processable NIR OPTs.

To compare the performance of NIR OPTs with a BHJ channel layer, a detailed summary is prepared in Table S1. Beside the BHJ channel, it shows that a high mobility channel combined with a light-sensitive BHJ absorber is another useful method to boost the detection performance in OPTs by separating the charge transport and charge photogeneration (Kim et al., 2019a; Li et al., 2021; Rim et al., 2015a). However, there are limitations in such structures, e.g., the solution erosion on the underlying film during the bilayer channel fabrication, and complex fabrication that would increase the cost. As shown in Table S1, the NIR OPTs with a DPP-DTT:$PC_{71}BM$-based BHJ channel exhibits very good charge mobility (~1 $cm^2V^{-1}s^{-1}$), which is essential for fast charge collection. The hole mobility is one of the highest among NIR OPTs with a BHJ channel. Decent photoresponsivity, specific detectivity, and response speed are also achieved, which can be further

improved by engineering the channel length and width and/or incorporate photonic structures in the PT (Lan et al., 2018; Li et al., 2019a).

DISCUSSION

In summary, the effect of acceptors on the electrical and optical properties of the NIR OPTs with an NIR absorbing BHJ channel layer has been systematically investigated. The introduction of a proper n-type acceptor into the p-type polymer channel would simultaneously improve the electrical ideality and photoresponse of the OPTs. The acceptor domain inside the BHJ not only reduces the contact resistance but also is capable of trapping the injected electrons, which avoids the electrons being trapped at the SiO_2/channel interface, leading to mitigated nonideality of the charge transport. Meanwhile, the donor/acceptor interface in the BHJ largely facilitates the photogenerated exciton dissociation and charge separation, resulting in enhanced NIR light responsivity and sensitivity in the OPTs. The results of this work provide an effect approach for improving the electrical ideality in NIR OPTs, enabling high-performance NIR detectors for practical applications.

Limitations of the study

Though the OPT devices showed a stable characteristic in ambient air, storing the devices in a dry box or a glovebox with inert atmosphere is preferred to keep the device performances.

STAR★METHODS

Detailed methods are provided in the online version of this paper and include the following:

- KEY RESOURCES TABLE
- RESOURCE AVAILABILITY
  - Lead contact
  - Materials availability
  - Data and code availability
- METHOD DETAILS
  - Material preparation
  - Device fabrication
  - Device characterization

SUPPLEMENTAL INFORMATION

Supplemental information can be found online at https://doi.org/10.1016/j.isci.2021.103711.

ACKNOWLEDGMENTS

The authors acknowledge financial support from General Research Fund from Research Grants Council of Hong Kong Special Administrative Region (GRF/12303920); NSFC/RGC Joint Research Scheme (N_HKBU201/19); Key R&D program of Shanxi Province (International Cooperation, 201903D421087); and Program for the Innovative Talents of Higher Education Institutions of Shanxi.

AUTHOR CONTRIBUTIONS

N. L., Y. M., and F. Z. conceived the idea, designed the experiments, and analyzed the data. N. L. carried out most of the fabrication and measurement of the devices. Y. L. conducted the contact resistance measurements and data analysis. All authors made a substantial contribution to the discussion of the content and writing of the manuscript.

DECLARATION OF INTERESTS

The authors declare no competing interests.

Received: October 20, 2021
Revised: December 12, 2021
Accepted: December 28, 2021
Published: January 21, 2022

SUPPORTING CITATIONS

The following references appear in the Supplemental Information: Nam et al. (2017); Rim et al., (2015b).

REFERENCES

Aguirre, C.M., Levesque, P.L., Paillet, M., Lapointe, F., St-Antoine, B.C., Desjardins, P., and Martel, R. (2009). The role of the oxygen/water redox couple in suppressing electron conduction in field-effect transistors. Adv. Mater. *21*, 3087–3091. https://doi.org/10.1002/adma.200900550.

Benduhn, J., Tvingstedt, K., Piersimoni, F., Ullbrich, S., Fan, Y., Tropiano, M., McGarry, K.A., Zeika, O., Riede, M.K., Douglas, C.J., et al. (2017). Intrinsic non-radiative voltage losses in fullerene-based organic solar cells. Nat. Energy *2*, 1–6. https://doi.org/10.1038/nenergy.2017.53.

Bittle, E.G., Basham, J.I., Jackson, T.N., Jurchescu, O.D., and Gundlach, D.J. (2016). Mobility overestimation due to gated contacts in organic field-effect transistors. Nat. Commun. *7*, 1–7. https://doi.org/10.1038/ncomms10908.

Bobbert, P.A., Sharma, A., Mathijssen, S.G.J., Kemerink, M., and De Leeuw, D.M. (2012). Operational stability of organic field-effect transistors. Adv. Mater. *24*, 1146–1158. https://doi.org/10.1002/adma.201104580.

Braga, D., and Horowitz, G. (2009). High-Performance organic field-effect transistors. Adv. Mater. *21*, 1473–1486. https://doi.org/10.1002/adma.200802733.

Chen, M., Lu, H., Abdelazim, N.M., Zhu, Y., Wang, Z., Ren, W., Kershaw, S.V., Rogach, A.L., and Zhao, N. (2017). Mercury telluride quantum dot based phototransistor enabling high-sensitivity room-temperature photodetection at 2000 nm. ACS Nano *11*, 5614–5622. https://doi.org/10.1021/acsnano.7b00972.

Chua, L., Zaumseil, J., Chang, J., and Ou, E.C. (2005). General observation of n-type field-effect behaviour in organic semiconductors. Nature *434*, 194–199. https://doi.org/10.1038/nature03293.1.

Fuentes-Hernandez, C., Chou, W.F., Khan, T.M., Diniz, L., Lukens, J., Larrain, F.A., Rodriguez-Toro, V.A., and Kippelen, B. (2020). Large-area low-noise flexible organic photodiodes for detecting faint visible light. Science *370*, 698–701. https://doi.org/10.1126/science.aba2624.

Gil, H.M., Price, T.W., Chelani, K., Bouillard, J.S.G., Calaminus, S.D.J., and Stasiuk, G.J. (2021). NIR-quantum dots in biomedical imaging and their future. iScience *24*, 102189. https://doi.org/10.1016/j.isci.2021.102189.

Guo, K., Righetto, M., Minotto, A., Zampetti, A., and Cacialli, F. (2021). Non-toxic near-infrared light-emitting diodes. iScience *24*, 102545. https://doi.org/10.1016/j.isci.2021.102545.

Guo, Y., Du, C., Di, C.A., Zheng, J., Sun, X., Wen, Y., Zhang, L., Wu, W., Yu, G., and Liu, Y. (2009). Field dependent and high light sensitive organic phototransistors based on linear asymmetric organic semiconductor. Appl. Phys. Lett. *94*, 100. https://doi.org/10.1063/1.3115794.

Han, H., Nam, S., Seo, J., Lee, C., Kim, H., Bradley, D.D.C., Ha, C.S., and Kim, Y. (2015). Broadband All-polymer phototransistors with nanostructured bulk heterojunction layers of NIR-sensing n-type and visible light-sensing p-type polymers. Sci. Rep. *5*, 1–13. https://doi.org/10.1038/srep16457.

Heeger, A.J. (2014). 25th anniversary article: bulk heterojunction solar cells: understanding the mechanism of operation. Adv. Mater. *26*, 10–28. https://doi.org/10.1002/adma.201304373.

Huo, N., Yang, S., Wei, Z., Li, S.-S., Xia, J.-B., and Li, J. (2015). Photoresponsive and gas sensing field-effect transistors based on multilayer WS2 nanoflakes. Sci. Rep. *4*, 5209. https://doi.org/10.1038/srep05209.

Hwang, D.K., Lee, Y.T., Lee, H.S., Lee, Y.J., Shokouh, S.H., Kyhm, J.H., Lee, J., Kim, H.H., Yoo, T.H., Nam, S.H., et al. (2016). Ultrasensitive PbS quantum-dot-sensitized InGaZnO hybrid photoinverter for near-infrared detection and imaging with high photogain. NPG Asia Mater. *8*, e233. https://doi.org/10.1038/am.2015.137.

Kim, C.H., Bonnassieux, Y., and Horowitz, G. (2013). Charge distribution and contact resistance model for coplanar organic field-effect transistors. IEEE Trans. Electron. Devices *60*, 280–287. https://doi.org/10.1109/TED.2012.2226887.

Kim, H., Wu, Z., Eedugurala, N., Azoulay, J.D., and Ng, T.N. (2019a). Solution-processed phototransistors combining organic absorber and charge transporting oxide for visible to infrared light detection. ACS Appl. Mater. Inter. *11*, 36880–36885. https://doi.org/10.1021/acsami.9b08622.

Kim, H., Wu, Z., Eedugurala, N., Azoulay, J.D., and Ng, T.N. (2019b). Solution-processed phototransistors combining organic absorber and charge transporting oxide for visible to infrared light detection. ACS Appl. Mater. Inter. *11*, 36880–36885. https://doi.org/10.1021/acsami.9b08622.

Kim, M.J., Choi, S., Lee, M., Heo, H., Lee, Y., Cho, J.H., and Kim, B. (2017). Photoresponsive transistors based on a dual acceptor-containing low-bandgap polymer. ACS Appl. Mater. Inter. *9*, 19011–19020. https://doi.org/10.1021/acsami.7b03058.

Knobelspies, S., Daus, A., Cantarella, G., Petti, L., Münzenrieder, N., Tröster, G., and Salvatore, G.A. (2016). Flexible a-IGZO phototransistor for instantaneous and cumulative UV-exposure monitoring for skin health. Adv. Electron. Mater. *2*, 1600273. https://doi.org/10.1002/aelm.201600273.

Lan, W., Wang, Y., Singh, J., and Zhu, F. (2018). Omnidirectional and broadband light absorption enhancement in 2-D photonic-structured organic solar cells. ACS Photon. *5*, 1144–1150. https://doi.org/10.1021/acsphotonics.7b01573.

Lan, Z., Lei, Y., Chan, W.K.E., Chen, S., Luo, D., and Zhu, F. (2020). Near-infrared and visible light dual-mode organic photodetectors. Sci. Adv. *6*, eaaw8065. https://doi.org/10.1126/sciadv.aaw8065.

Lei, Y., Deng, P., Li, J., Lin, M., Zhu, F., Ng, T.W., Lee, C.S., and Ong, B.S. (2016a). Solution-processed donor-acceptor polymer nanowire network semiconductors for high-performance field-effect transistors. Sci. Rep. *6*, 1–9. https://doi.org/10.1038/srep24476.

Lei, Y., Deng, P., Lin, M., Zheng, X., Zhu, F., and Ong, B.S. (2016b). Enhancing crystalline structural orders of polymer semiconductors for efficient charge transport via polymer-matrix-mediated molecular self-assembly. Adv. Mater. *28*, 6687–6694. https://doi.org/10.1002/adma.201600580.

Lei, Y., Li, N., Chan, W.K.E., Ong, B.S., and Zhu, F. (2017). Highly sensitive near infrared organic phototransistors based on conjugated polymer nanowire networks. Org. Electron. *48*, 12–18. https://doi.org/10.1016/j.orgel.2017.05.029.

Lei, Y., Wu, B., Chan, W.-K.E., Zhu, F., and Ong, B.S. (2015). Engineering gate dielectric surface properties for enhanced polymer field-effect transistor performance. J. Mater. Chem. C *3*, 12267–12272. https://doi.org/10.1039/C5TC02579F.

Li, F., Chen, Y., Ma, C., Buttner, U., Leo, K., and Wu, T. (2017). High-performance near-infrared phototransistor based on n-type small-molecular organic semiconductor. Adv. Electron. Mater. *3*, 1600430. https://doi.org/10.1002/aelm.201600430.

Li, J., Zhao, Y., Tan, H.S., Guo, Y., Di, C.A., Yu, G., Liu, Y., Lin, M., Lim, S.H., Zhou, Y., et al. (2012). A stable solution-processed polymer semiconductor with record high-mobility for printed transistors. Sci. Rep. *2*, 1–9. https://doi.org/10.1038/srep00754.

Li, N., Eedugurala, N., Leem, D.S., Azoulay, J.D., and Ng, T.N. (2021a). Organic upconversion imager with dual electronic and optical readouts for shortwave infrared light detection. Adv. Funct. Mater. *31*, 2100565. https://doi.org/10.1002/adfm.202100565.

Li, N., Lan, W., Lau, Y.S., Cai, L., Syed, A.A., and Zhu, F. (2019a). Enhanced long wavelength omnidirectional photoresponses in photonic-structured perovskite photodetectors. J. Mater. Chem. C *7*, 9573–9580. https://doi.org/10.1039/c9tc02149c.

Li, N., Lan, Z., Cai, L., and Zhu, F. (2019b). Advances in solution-processable near-infrared phototransistors. J. Mater. Chem. C *7*, 3711–3729. https://doi.org/10.1039/c8tc06078a.

Li, N., Lan, Z., Lau, Y.S., Xie, J., Zhao, D., and Zhu, F. (2020). SWIR photodetection and visualization realized by incorporating an organic SWIR sensitive bulk heterojunction. Adv. Sci. *7*, 2000444. https://doi.org/10.1002/advs.202000444.

Li, N., Lau, Y.S., Xiao, Z., Ding, L., and Zhu, F. (2018). NIR to visible light upconversion devices

comprising an NIR charge generation layer and a perovskite emitter. Adv. Opt. Mater. *6*, 1801084. https://doi.org/10.1002/adom.201801084.

Li, N., Lei, Y., Chan, W.K.E., and Zhu, F. (2019c). Broadband phototransistors realised by incorporating a bi-layer perovskite/NIR light absorbing polymer channel. J. Mater. Chem. C *7*, 4808–4816. https://doi.org/10.1039/c8tc06229c.

Li, N., Mahalingavelar, P., Vella, J.H., Leem, D.S., Azoulay, J.D., and Ng, T.N. (2021b). Solution-processable infrared photodetectors: materials, device physics, and applications. Mater.Sci. Eng. R. Rep. *146*, 100643. https://doi.org/10.1016/j.mser.2021.100643.

Li, Q., Ran, Y., Shi, W., Qin, M., Sun, Y., Kuang, J., Wang, H., Chen, H., Guo, Y., and Liu, Y. (2021). High-performance near-infrared polymeric phototransistors realized by combining cross-linked polymeric semiconductors and bulk heterojunction bilayer structures. Appl. Mater. Today *22*, 100899. https://doi.org/10.1016/j.apmt.2020.100899.

Liu, C., Li, G., Di Pietro, R., Huang, J., Noh, Y.Y., Liu, X., and Minari, T. (2017). Device physics of contact issues for the overestimation and underestimation of carrier mobility in field-effect transistors. Phys. Rev. Appl. *8*. https://doi.org/10.1103/PhysRevApplied.8.034020.

Liu, S., Yuan, J., Deng, W., Luo, M., Xie, Y., Liang, Q., Zou, Y., He, Z., Wu, H., and Cao, Y. (2020). High-efficiency organic solar cells with low non-radiative recombination loss and low energetic disorder. Nat. Photon. *14*, 300–305. https://doi.org/10.1038/s41566-019-0573-5.

Liu, X., Guo, Y., Ma, Y., Chen, H., Mao, Z., Wang, H., Yu, G., and Liu, Y. (2014). Flexible, low-voltage and high-performance polymer thin-film transistors and their application in photo/thermal detectors. Adv. Mater. *26*, 3631–3636. https://doi.org/10.1002/adma.201306084.

Luo, C., Ko, A., Kyaw, K., Perez, L.A., Patel, S., Wang, M., Grimm, B., Bazan, G.C., Kramer, E.J., and Heeger, A.J. (2014). General strategy for self-assembly of highly oriented nanocrystalline semiconducting polymers with high mobility. Nano Lett. *14*, 2764–2771.

McCulloch, I., Salleo, A., and Chabinyc, M. (2016). Avoid the kinks when measuring mobility. Science *352*, 1521–1522. https://doi.org/10.1126/science.aaf9062.

Nam, S., Han, H., Seo, J., Song, M., Kim, H., Anthopoulos, T.D., McCulloch, I., Bradley, D.D.C., and Kim, Y. (2016). Ambipolar organic phototransistors with p-Type/n-Type conjugated polymer bulk heterojunction light-sensing layers. Adv. Electron. Mater. *2*, 1600264. https://doi.org/10.1002/aelm.201600264.

Nam, S., Seo, J., Han, H., Kim, H., Bradley, D.D.C., and Kim, Y. (2017). Efficient deep red light-sensing all-polymer phototransistors with p-type/n-type conjugated polymer bulk heterojunction layers. ACS Appl. Mater. Inter. *9*, 14983–14989. https://doi.org/10.1021/acsami.7b01983.

Newman, C.R., Frisbie, C.D., Da Silva Filho, D.A., Brédas, J.L., Ewbank, P.C., and Mann, K.R. (2004). Introduction to organic thin film transistors and design of n-channel organic semiconductors. Chem. Mater. *16*, 4436–4451. https://doi.org/10.1021/cm049391x.

Ng, T.N., Chabinyc, M.L., Street, R.A., and Salleo, A. (2007). Bias stress effects in organic thin film transistors. 2007 IEEE International Reliability Physics Symposium Proceedings. 45th Annual, pp. 243–247.

Nikolka, M., Nasrallah, I., Rose, B., Ravva, M.K., Broch, K., Sadhanala, A., Harkin, D., Charmet, J., Hurhangee, M., Brown, A., et al. (2017). High operational and environmental stability of high-mobility conjugated polymer field-effect transistors through the use of molecular additives. Nat. Mater. *16*, 356–362. https://doi.org/10.1038/nmat4785.

Osedach, T.P., Zhao, N., Geyer, S.M., Chang, L.Y., Wanger, D.D., Arango, A.C., Bawendi, M.C., and Bulović, V. (2010). Interfacial recombination for fast operation of a planar organic/QD infrared photodetector. Adv. Mater. *22*, 5250–5254. https://doi.org/10.1002/adma.201002589.

Park, S.H., Roy, A., Beaupré, S., Cho, S., Coates, N., Moon, J.S., Moses, D., Leclerc, M., Lee, K., and Heeger, A.J. (2009). Bulk heterojunction solar cells with internal quantum efficiency approaching 100%. Nat. Photon. *3*, 297–303. https://doi.org/10.1038/nphoton.2009.69.

Pham, N.D., Tiong, V.T., Chen, P., Wang, L., Wilson, G.J., Bell, J., and Wang, H. (2017). Enhanced perovskite electronic properties via a modified lead(ii) chloride Lewis acid-base adduct and their effect in high-efficiency perovskite solar cells. J. Mater. Chem. A. *5*, 5195–5203. https://doi.org/10.1039/c6ta11139d.

Phan, H., Ford, M.J., Lill, A.T., Wang, M., Bazan, G.C., and Nguyen, T.Q. (2018). Electrical double-slope nonideality in organic field-effect transistors. Adv. Funct. Mater. *28*, 1707221. https://doi.org/10.1002/adfm.201707221.

Phan, H., Ford, M.J., Lill, A.T., Wang, M., Bazan, G.C., and Nguyen, T.Q. (2017). Improving electrical stability and ideality in organic field-effect transistors by the addition of fullerenes: understanding the working mechanism. Adv. Funct. Mater. *27*, 1701358. https://doi.org/10.1002/adfm.201701358.

Phan, H., Wang, M., Bazan, G.C., and Nguyen, T.Q. (2015). Electrical instability induced by electron trapping in low-bandgap donor-acceptor polymer field-effect transistors. Adv. Mater. *27*, 7004–7009. https://doi.org/10.1002/adma.201501757.

Pierre, A., Gaikwad, A., and Arias, A.C. (2017). Charge-integrating organic heterojunction phototransistors for wide-dynamic-range image sensors. Nat. Photon. *11*, 193–199. https://doi.org/10.1038/nphoton.2017.15.

Qian, D., Zheng, Z., Yao, H., Tress, W., Hopper, T.R., Chen, Shula, Li, S., Liu, J., Chen, Shangshang, Zhang, J., et al. (2018). Design rules for minimizing voltage losses in high-efficiency organic solar cells. Nat. Mater. *17*, 703–709. https://doi.org/10.1038/s41563-018-0128-z.

Rim, Y.S., Yang, Y., Bae, S.H., Chen, H., Li, C., Goorsky, M.S., and Yang, Y. (2015a). Ultrahigh and broad spectral photodetectivity of an organic-inorganic hybrid phototransistor for flexible electronics. Adv. Mater. *27*, 6885–6891. https://doi.org/10.1002/adma.201502996.

Rim, Y.S., Yang, Y.M., Bae, S., Chen, H., Li, C., Goorsky, M.S., and Yang, Y. (2015b). Ultrahigh and broad spectral photodetectivity of an organic – inorganic hybrid phototransistor for flexible electronics. Adv. Mater. *27*, 6885–6891. https://doi.org/10.1002/adma.201502996.

Scharber, M.C., Mühlbacher, D., Koppe, M., Denk, P., Waldauf, C., Heeger, A.J., and Brabec, C.J. (2006). Design rules for donors in bulk-heterojunction solar cells - towards 10 % energy-conversion efficiency. Adv. Mater. *18*, 789–794. https://doi.org/10.1002/adma.200501717.

Shen, L., Fang, Y., Wang, D., Bai, Y., Deng, Y., Wang, M., Lu, Y., and Huang, J. (2016). A self-powered, sub-nanosecond-response solution-processed hybrid perovskite photodetector for time-resolved photoluminescence-lifetime detection. Adv. Mater. *28*, 10794–10800. https://doi.org/10.1002/adma.201603573.

Sirringhaus, H. (2014). 25th anniversary article: organic field-effect transistors: the path beyond amorphous silicon. Adv. Mater. *26*, 1319–1335. https://doi.org/10.1002/adma.201304346.

Sun, Z., Li, J., and Yan, F. (2012). Highly sensitive organic near-infrared phototransistors based on poly(3-hexylthiophene) and PbS quantum dots. J. Mater. Chem. *22*, 21673–21678. https://doi.org/10.1039/c2jm34773c.

Wang, C., Ren, X., Xu, C., Fu, B., Wang, R., Zhang, X., Li, R., Li, H., Dong, H., Zhen, Y., et al. (2018). N-type 2D organic single crystals for high-performance organic field-effect transistors and near-infrared phototransistors. Adv. Mater. *30*, 1706260. https://doi.org/10.1002/adma.201706260.

Wang, D., Qin, R., Zhou, G., Li, X., Xia, R., Li, Y., Zhan, L., Zhu, H., Lu, X., Yip, H.L., et al. (2020). High-performance semitransparent organic solar cells with excellent infrared reflection and see-through functions. Adv. Mater. *32*, 1–8. https://doi.org/10.1002/adma.202001621.

Wei, Y., Ren, Z., Zhang, A., Mao, P., Li, H., Zhong, X., Li, W., Yang, S., and Wang, J. (2018). Hybrid organic/PbS quantum dot bilayer photodetector with low dark current and high detectivity. Adv. Funct. Mater. *28*, 1706690. https://doi.org/10.1002/adfm.201706690.

Xie, B., Xie, R., Zhang, K., Yin, Q., Hu, Z., Yu, G., Huang, F., and Cao, Y. (2020). Self-filtering narrowband high performance organic photodetectors enabled by manipulating localized Frenkel exciton dissociation. Nat. Commun. *11*, 2871. https://doi.org/10.1038/s41467-020-16675-x.

Xu, H., Li, J., Leung, B.H.K., Poon, C.C.Y., Ong, B.S., Zhang, Y., and Zhao, N. (2013a). A high-sensitivity near-infrared phototransistor based on an organic bulk heterojunction. Nanoscale *5*, 11850. https://doi.org/10.1039/c3nr03989g.

Xu, H., Li, J., Leung, B.H.K., Poon, C.C.Y., Ong, B.S., Zhang, Y., and Zhao, N. (2013b). A high-sensitivity near-infrared phototransistor based on an organic bulk heterojunction. Nanoscale *5*, 11850–11855. https://doi.org/10.1039/c3nr03989g.

Xu, H., Liu, J., Zhang, J., Zhou, G., Luo, N., and Zhao, N. (2017). Flexible organic/inorganic hybrid near-infrared photoplethysmogram sensor for cardiovascular monitoring. Adv. Mater. *29*, 1700975. https://doi.org/10.1002/adma.201700975.

Xu, H., Zhu, Q., Wu, T., Chen, W., Zhou, G., Li, J., Zhang, H., and Zhao, N. (2016). An organic water-gated ambipolar transistor with a bulk heterojunction active layer for stable and tunable photodetection. Appl. Phys. Lett. *109*, 213301. https://doi.org/10.1063/1.4968580.

Yokota, T., Nakamura, T., Kato, H., Mochizuki, M., Tada, M., Uchida, M., Lee, S., Koizumi, M., Yukita, W., Takimoto, A., and Someya, T. (2020). A conformable imager for biometric authentication and vital sign measurement. Nat. Electron. *3*, 113–121. https://doi.org/10.1038/s41928-019-0354-7.

Yu, H., Bao, Z., and Oh, J.H. (2013). High-performance phototransistors based on single-crystalline n-channel organic nanowires and photogenerated charge-carrier behaviors. Adv. Funct. Mater. *23*, 629–639. https://doi.org/10.1002/adfm.201201848.

Yu, K., Park, B., Kim, G., Kim, C.H., Park, S., Kim, Jehan, Jung, S., Jeong, S., Kwon, S., Kang, H., et al. (2016). Optically transparent semiconducting polymer nanonetwork for flexible and transparent electronics. Proc. Natl. Acad. Sci. U. S. A. *113*, 14261–14266. https://doi.org/10.1073/pnas.1606947113.

Zaumseil, J., and Sirringhaus, H. (2007). Electron and ambipolar transport in organic field-effect transistors. Chem. Rev. *107*, 1296–1323. https://doi.org/10.1021/cr0501543.

Zheng, S., Chen, J., Johansson, E.M.J., and Zhang, X. (2020). PbS colloidal quantum dot inks for infrared solar cells. iScience *23*, 101753. https://doi.org/10.1016/j.isci.2020.101753.

Zhu, M., Lv, S., Wang, Q., Zhang, G., Lu, H., and Qiu, L. (2016). Enhanced near-infrared photoresponse of organic phototransistors based on single-component donor-acceptor conjugated polymer nanowires. Nanoscale *8*, 7738–7748. https://doi.org/10.1039/c5nr09003b.

STAR★METHODS

KEY RESOURCES TABLE

REAGENT or RESOURCE	SOURCE	IDENTIFIER
Chemicals, peptides, and recombinant proteins		
DPP-DTT	Ossila	CAS No.1260685-66-2
$PC_{61}BM$	Sigma Aldrich	CAS No. 160848-22-6
$PC_{71}BM$	Sigma Aldrich	CAS No. 609771-63-3
ITIC	Solarmer	http://www.solarmer-materials.com/index.php?_m%20=%20mod_product&_a%20=%20view&p_id%20=%20989
1, 2-Dichlorobenzene	Sigma Aldrich	CAS No. 95-50-1
Software and algorithms		
MATLAB R2019b	This paper	https://www.mathworks.com/products/matlab-home.html

RESOURCE AVAILABILITY

Lead contact

Further information and requests for resources and reagents should be directed to and will be fulfilled by the Lead Contact, Yanqin Miao (miaoyanqin@tyut.edu.cn).

Materials availability

This study did not generate new unique reagents.

Data and code availability

- Any data reported will be shared by the lead contact upon request.
- Any code used for data analysis will be provided by the lead contact upon request.
- Any additional information required to reanalyze the data is available from the lead contact upon request.

METHOD DETAILS

Material preparation

The polymer diketopyrrolopyrrole-dithienylthieno[3,2-b]thiophene (DPP-DTT, from Ossila) was selected as the NIR donor with a peak absorption at 820 nm (Li et al., 2012). The acceptor materials, [6,6]-Phenyl-C61-butyric acid methyl ester ($PC_{61}BM$), [6,6]-Phenyl-C71-butyric acid methyl ester ($PC_{71}BM$) were purchased from Sigma Aldrich, and 3,9-bis(2-methylene-(3-(1,1-dicyanomethylene)-indanone))-5,5,11,11-tetrakis(4-hexylphenyl)-dithieno[2,3-d:2′,3′-d′]-s-indaceno[1,2-b:5,6-b′]dithiophene (ITIC) was ordered from Solarmer. The BHJ solutions were prepared by mixing 4 mg/mL DPP-DTT polymer and 2 mg/mL acceptor material in 1, 2-Dichlorobenzene. The donor/acceptor mixture solutions were kept stirring and heating at 60°C overnight before use.

Device fabrication

Heavily p-doped silicon substrates with a 300 nm thick thermally grown SiO_2 layer were ultrasonically cleaned in deionized water, acetone and isopropyl alcohol respectively and then dried in oven. The capacitance per unit area of the SiO_2 gate dielectric layer C_i is ~10 nF/cm^2.

The surface of the SiO_2 layer was first treated with trichloro(octadecyl)silane to passivate the surface defects (Lei et al., 2015, 2017). This self-assembled monolayer formation method is a silylation process via solution treatment. After sonification cleaning, the SiO_2 substrates are immersed in a dilute solution of the silylating agent, followed by solvent rinsing and air drying.

The spin coating was performed in a glovebox with O_2 and H_2O levels below 0.1 ppm. The active layers were ~50 nm in thickness. After spin coating, the organic semiconductor thin films were annealed at 180°C for 10 min in the glovebox to improve the molecular packing. A ~40 nm thick gold (Au) top contact was deposited using thermal evaporation in vacuum using a shadow mask, which also defines a channel length of 80 μm and width of 1500 μm.

Device characterization

The photoresponse characteristics for the NIR OPTs were measured in ambient without encapsulation. An NIR LED with a peak emission of 850 nm was used as the NIR light source in the measurement. The light intensity was controlled by optical filters (Thorlabs) and calibrated by optical power meters (Thorlabs). The voltage applied to the OPT was provided by a Keithley sourcemeter (2636B), where the current was simultaneously recorded. The PL characteristics of the NIR channel layers used in the OPTs were measured under a pulsed 325 nm laser in ambient. The PL signal was amplified before it was recorded.